

See discussions, stats, and author profiles for this publication at: <https://www.researchgate.net/publication/10999361>

Assembly of Amyloid Protofibrils via Critical Oligomers—A Novel Pathway of Amyloid Formation

ARTICLE *in* JOURNAL OF MOLECULAR BIOLOGY · FEBRUARY 2003

Impact Factor: 4.33 · DOI: 10.1016/S0022-2836(02)01175-0 · Source: PubMed

CITATIONS

137

READS

86

4 AUTHORS, INCLUDING:



[Andreas Modler](#)

Zurich University of Applied Sciences

6 PUBLICATIONS 317 CITATIONS

SEE PROFILE



Assembly of Amyloid Protofibrils *via* Critical Oligomers—A Novel Pathway of Amyloid Formation

A. J. Modler^{1,2*}, K. Gast², G. Lutsch² and G. Damaschun^{1,2}

¹*Institut für Biologie c/o
Max-Delbrück-Centrum für
Molekulare Medizin
Humboldt-Universität zu
Berlin, Robert-Rössle-Strasse
10, D-13092 Berlin PF 740238
Germany*

²*Max-Delbrück-Centrum für
Molekulare Medizin, D-13092
Berlin, Germany*

The amyloid formation of phosphoglycerate kinase (PGK) was investigated by static and dynamic light-scattering. The time-course of the scattering intensity and the hydrodynamic radius scale with initial monomer concentration in a linear fashion over a range of about 50 in concentration. This sets limits on theories for aggregation kinetics that can be used, and points towards irreversible, cascade type models. In addition, circular dichroism (CD) was used to monitor the transition between a predominantly α -helical spectrum to a β -sheet enriched one. The time-course of the CD also proves to scale linearly with initial monomer concentration. Electron microscopy shows that small oligomers as well as protofibrils are present during aggregation. The found coupling between growth of intermediates and acquisition of β -sheet structure is interpreted in terms of a generalized diffusion–collision model, where stabilization of β -strands takes place by intermolecular interactions.

© 2002 Elsevier Science Ltd. All rights reserved

Keywords: amyloid; misfolding; non-native structure; diffusion–collision; colloid

*Corresponding author

Introduction

The misfolding and aggregation of proteins is a topic of outstanding interest due to its significance during processing of proteins in biotechnology and the occurrence of protein deposits in a variety of diseases.¹ These diseases include the amyloidoses,² the most prominent neurodegenerative diseases like Alzheimer's and Parkinson's disease and the prion diseases.³ All protein deposits connected with disease are characterized by enriched cross β -sheet structure and are referred to as amyloid or amyloid-like if they show fibrillar morphology.¹ During the final stages of systemic amyloidosis amyloid plaques lead to dysfunction and rupture of organs.² Whether the mechanism of protein aggregation and deposition

is an epiphenomenon or a cause of neurodegenerative diseases is a matter of debate,^{4,5} apart from the prion diseases where overwhelming experimental evidence suggests that protein deposits or their precursors are the infectious agents responsible for transmission of disease.³

A detailed understanding of the underlying molecular mechanisms of amyloid or prion formation is an essential step for developing diagnostic tests and therapeutic strategies.⁶

The nucleation polymerization mechanism (NP)⁷ was the first model used for rationalizing the results of *in vitro* experiments probing the kinetics of amyloid formation and simultaneously addressing the mechanism of infection during prion diseases.⁸ Prusiner's originally proposed heterodimer mechanism⁹ was shown to give rise to rather unrealistic predictions, whereas generalizations of the model are phenomenologically equivalent to the nucleation polymerization mechanism.¹⁰ The results of a recent biophysical study of the kinetics of amyloid formation of the C-terminal truncated region of yeast prion protein Sup35 (NM) are not consistent with a sole nucleation polymerization mechanism.¹¹ The authors proposed a new model called nucleated conformational conversion (NCC) which stresses the role of association-competent oligomeric intermediates which results in an additional kinetic pathway *via* clustering of the oligomeric species. From atomic

Abbreviations used: PGK, phosphoglycerate kinase; SLS, static light-scattering; DLS, dynamic light-scattering; CD, circular dichroism; NP, nucleated polymerization; NCC, nucleated conformational conversion; UV, ultraviolet; NM, C-terminal truncated region of the yeast prion protein Sup35; IgG, immunoglobulin; TTR, transthyretin; PrP, prion protein; DLCA, diffusion limited cluster aggregation; RLCA, reaction limited cluster aggregation; XOVER, cross-over regime; CtCO, clustering towards critical oligomers; CoCO, clustering of critical oligomers.

E-mail address of the corresponding author: modler@mdc-berlin.de

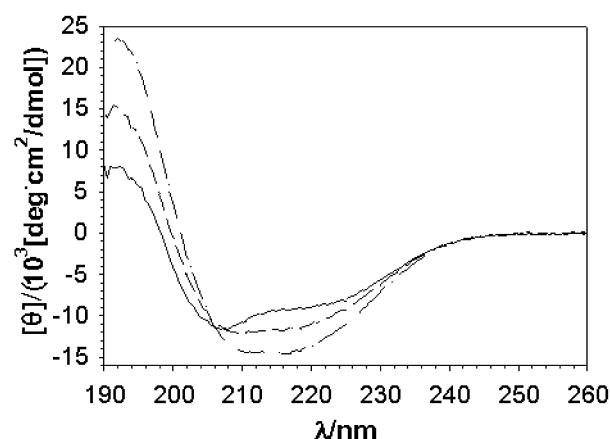


Figure 1. Far-UV CD spectra of PGK ($n_1 = 21.8 \mu\text{M}$) monitored in 190 mM NaCl (pH 2), 10 mM HCl at different times during amyloid protofibril formation. Immediately after the start of experiment (—), after 14 hours (---) and after 144 hours (— · —).

force measurements with the same protein construct, Xu *et al.*¹² independently derived a similar concept of the assembly of so-called nucleation units. They hypothesize that the assembly behavior of these nucleation units is analogous to linear colloidal aggregation. The latest reviews also emphasize the importance of soluble oligomeric aggregates of A β and α -synuclein in the case of Alzheimer's and Parkinson's disease, respectively. These are assumed to be the primary neurotoxic agents which could solve the puzzle of the weak correlation between fibrillar amyloid load and neurological dysfunction.^{5,13}

The motivation for this contribution was to undertake the above mentioned models of amyloid formation a critical testing. Yeast phosphoglycerate kinase (PGK) was chosen as model system for this purpose. PGK, among other non-disease related proteins¹⁴ was recently shown to adopt a partially folded intermediate state¹⁵ which initiates its conversion into amyloid-like structures.^{15,16}

The fibrillogenesis of PGK is a two-step process but one which is characterized by the absence of a nucleation event. This is shown by systematic monitoring of the concentration and time-dependence of the size and mass of the growing protein species, using static (SLS) and dynamic light-scattering (DLS), circular dichroism (CD) and by electron microscopy. In the first stage of fibril formation a critical oligomer or an ensemble of critical oligomers is built up. In the second stage the oligomers aggregate into protofibrillar structures. Within the resolution of the experiments both stages can be very well rationalized on the basis of colloid coagulation theory^{17,18} and its generalizations.¹⁹

The derived model of amyloid formation is compared to the existing models, cited above. The relationship of the different pathways, on which the models are founded, is discussed.

Results

In this section we first characterize the initial state of PGK. It is confirmed that the final aggregates formed in the experiments are structures fulfilling all criteria to call them amyloid. The results on the kinetics of amyloid formation, measured by means of SLS, DLS and CD, are then summarized. The consensus of these experimental results derived by the different methods lead us to propose a new model of amyloid formation.

Characterization of initial and aggregated states of PGK

The initial state of PGK leading to amyloid formation was induced by adding NaCl to the acid-unfolded state of PGK. The resulting solvent conditions were 10 mM HCl (pH 2), 190 mM NaCl for all protein concentrations, except for one experiment at a protein concentration of $n_1 = 60.6 \mu\text{M}$ which was carried out in $^2\text{H}_2\text{O}$ (pH 2) instead of H_2O . Monomer concentrations of protein are given in molar units and denoted as n_1 throughout the text. The acid-unfolded state has been characterized in detail.¹⁵

The concentration dependence of the diffusion coefficient and the molar mass of the anion-induced, partially refolded state of PGK was measured (data not shown). Extrapolation to zero concentration yields a molar mass of $48,510 \text{ g mol}^{-1}$ which is within 10% of the chemical value of $M = 44,570 \text{ g mol}^{-1}$, indicating a monomeric initial state. Linear regression of the experimental data for the diffusion coefficient resulted in $D = D_0(1 + k_D \times n_1) = 5.11(1 - 7443.19n_1) \times 10^{-7} \text{ cm}^2 \text{ s}^{-1}$. The hydrodynamic radius, R_S , was calculated to be $4.2(\pm 0.2) \text{ nm}$, using the Stokes-Einstein equation $R_S = k_B T / 6\pi\eta D$, where k_B denotes Boltzmann's constant, T , the temperature, and η , the solvent viscosity, and using $D_0 = 5.11(\pm 0.26) \times 10^{-7} \text{ cm}^2 \text{ s}^{-1}$. This value lies between those of the native state, $R_S = 2.97 \text{ nm}$, and the acid-unfolded state, $R_S = 7.42(\pm 0.08) \text{ nm}$ ¹⁵ providing evidence for a collapsed initial state. R_S is the hydrodynamic radius corresponding to the radius of a sphere having the same translational diffusion coefficient as the investigated particles of arbitrary shape would have. The value is thus a phenomenological quantity but no further model assumption is used.

The far-ultraviolet (UV) CD spectrum of the initial state of PGK (Figure 1) is typical of an α -helical conformation, with minima around 208 nm and 222 nm. This indicates that the protein is folded and includes ordered helical secondary structure, justifying the term anion-induced partially refolded state.

In contrast the far-UV CD spectrum after incubation for 144 hours indicates a predominantly β -sheet structure with the typical minimum around 215 nm. Air-dried drops of the solution were stained with Congo red. This led to the

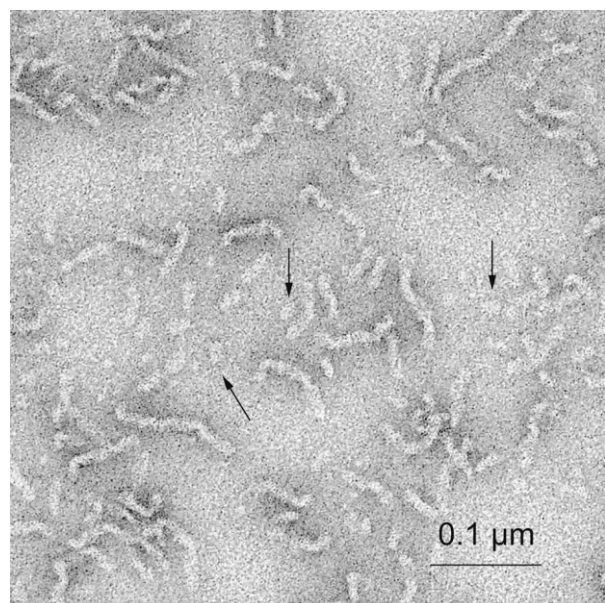


Figure 2. Electron micrograph of aggregated states of PGK. PGK at $21.8 \mu\text{M}$ in 190 mM NaCl ($\text{pH } 2$), 10 mM HCl was allowed to aggregate for 12 hours. It was then diluted 1:10 and stored at 4°C to prevent further aggregation prior to sample preparation for electron microscopy. Small oligomers are indicated by the arrows. Magnification $63,000\times$.

yellow-green birefringence that is characteristic of amyloid when investigated microscopically with crossed polarizers. Electron micrographs of negatively stained samples of the solution show fibrils with a diameter of about $8\text{--}9 \text{ nm}$ and a length distribution between 50 nm and 250 nm (data not shown). The appearance is similar to the fibrillar morphology obtained with trichloroacetate¹⁶. Cross β -structure of fibrils was confirmed by solution X-ray scattering through the presence of a characteristic diffraction peak at 4.7 \AA as reported.¹⁶

Figure 2 shows an electron micrograph taken at a time-point which corresponds approximately to the far-UV CD spectrum after 14 hours shown in Figure 1. Small oligomeric aggregates and short fibrils can be seen. The small oligomers have a spherical or ellipsoidal shape and presumably represent monomers up to pentamers. A maximum size of ten monomers can be taken as the limit for these oligomers. The short fibrils already have a diameter of $8\text{--}9 \text{ nm}$. At this stage the longest fibrils have a length of about 120 nm .

Static and dynamic light-scattering

We studied the kinetics of PGK amyloid formation at protein concentrations of $3.3 \mu\text{M}$, $21.8 \mu\text{M}$, $60.6 \mu\text{M}$, and $154.8 \mu\text{M}$ in 10 mM HCl and $60.6 \mu\text{M}$ in $10 \text{ mM } ^2\text{HCl}$. The concentration of salt was 190 mM NaCl in each case. The apparent average mass $M(t)$ was monitored by SLS (Figure 3(a)). The size of the growing species in terms of

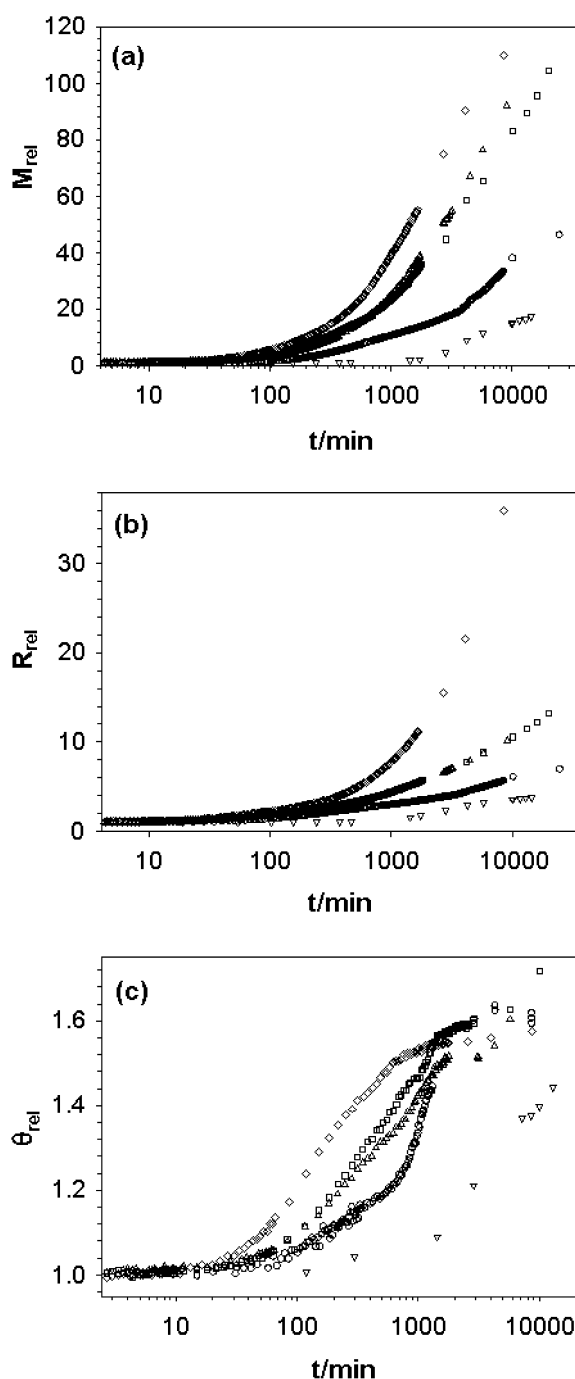


Figure 3. Kinetic measurements of PGK protofibril formation monitored by (a) SLS yielding $M_{\text{rel}}(t) = M(t)/M(0)$, (b) DLS yielding $R_{\text{rel}}(t) = R_S(t)/R_S(0)$ and (c) CD yielding $\theta_{\text{rel}} = \theta_{215}(t)/\theta_{215}(0)$. The corresponding concentrations were $3.3 \mu\text{M}$ (∇), $21.8 \mu\text{M}$ (\circ), $60.6 \mu\text{M}$ in $^2\text{H}_2\text{O}$ (\triangle), $60.6 \mu\text{M}$ (\square) and $154.8 \mu\text{M}$ (\diamond). The solvent conditions were 190 mM NaCl ($\text{pH } 2$), 10 mM HCl except the indicated kinetic run which was performed in $^2\text{H}_2\text{O}$ and 190 mM NaCl , $10 \text{ mM } ^2\text{HCl}$.

the apparent average hydrodynamic radius $R_S(t)$ was determined by DLS and calculated *via* the Stokes–Einstein equation from the apparent diffusion coefficient (Figure 3(b)). The apparent quantities $M_{\text{rel}}(t)$ and $R_{\text{rel}}(t)$ (Figure 3(a) and (b))

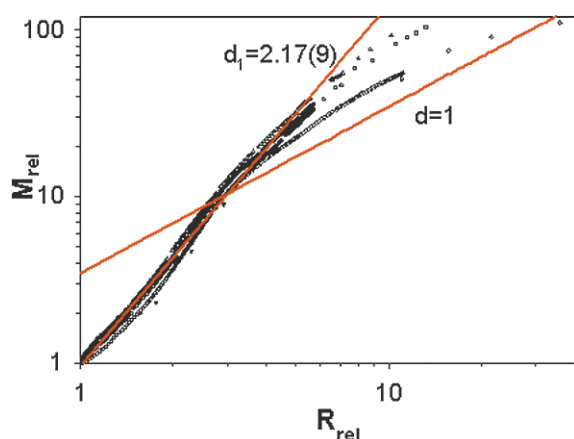


Figure 4. Double-logarithmic plot of the relative molar mass M_{rel} versus the relative Stokes radius R_{rel} for PGK. The concentrations were $3.3 \mu\text{M}$ (∇), $21.8 \mu\text{M}$ (\circ), $60.6 \mu\text{M}$ in $^2\text{H}_2\text{O}$ (\triangle), $60.6 \mu\text{M}$ (\square), and $154.8 \mu\text{M}$ (\diamond). Two growth regimes can be seen. The red lines indicate growth according to the scaling law $M_{\text{rel}} \propto R_{\text{rel}}^d$. The steeper straight line denoted by $d_1 = 2.17 \pm 0.09$ is the fit to the data in the interval $1 < M_{\text{rel}} < 10$. Strict linear growth starting from $M_{\text{rel}} = 10$ is shown by the line with $d = 1$.

are defined by the ratios $M_{\text{rel}}(t) = M(t)/M(0)$ and $R_{\text{rel}}(t) = R_S(t)/R_S(0)$, respectively, where $M(0)$ and $R_S(0)$ denote the initial apparent values at the start of the experiments. $M_{\text{rel}}(t)$ is a direct measure of the normalized mean cluster mass and therefore proportional to the second moment $\bar{n}(t) = \sum_i i^2 n_i(t)$ of the cluster size distribution $n_i(t)$. The term apparent is used to stress that the data is not extrapolated to zero concentration. Logarithmic time axes were chosen to combine all kinetic runs for the different concentrations in order to optimize the presentation of the essential characteristics of the data. A first inspection of the graphs reveals a concentration-dependent apparent lag-phase followed by a pronounced growth phase. The growth phase did not reach saturation, even in the longest run at $n_1 = 60.6 \mu\text{M}$ which was observed for 14 days. Some protein solutions were stored for up to six months and remained transparent for all the time. The absence of significant turbidity is a clear indication that multiple scattering can be disregarded.

Circular dichroism

The ellipticity at 215 nm was used to follow the change in secondary structure during the process of amyloid formation (Figure 3(c)). The measure $\theta_{\text{rel}}(t)$ is defined by $\theta_{\text{rel}}(t) = \theta_{215}(t)/\theta_{215}(0)$. Again a logarithmic time axis is chosen to combine all experiments. The solvent conditions and concentrations were the same as in the light-scattering studies. At the beginning there is only a slight change in the CD signal during the apparent concentration-dependent lag-phase in the light-scattering experiments. This phase is followed by

a drastic change in secondary structure where approximately all of the transition to a predominantly β -sheet structure occurs. A far-UV CD spectrum recorded at the end of this phase, six days after initiation of the experiment (Figure 1), displays all the characteristics of a β -sheet structure.

Phenomenological data analysis

Characteristics of the aggregated species participating in amyloid formation of PGK are extracted by plotting M_{rel} versus R_{rel} in a double-logarithmic graph. This procedure eliminates the time and reveals information about the dimensionality d of the amyloid growth process *via* the mass scaling law $M \propto R^d$, as can be seen in Figure 4. Two regimes are clearly distinguishable. Up to an average mass of ten monomers, the data for the different concentrations approximately superimpose. This first growth stage can be described phenomenologically by assigning an exponent of $d_1 = 2.17 \pm 0.09$, derived from fits assuming the mass scaling law. Bulk growth would be indicated by a dimension $d = 3$. For obvious reasons clusters in this size range cannot have packing sufficiently dense to give rise to pure bulk growth.

The transition towards the second regime starts roughly when the average mass exceeds ten monomers. The slopes of the curves decrease progressively falling below the value for two-dimensional growth. The second growth stage is fully established for average cluster masses larger than 30 monomer masses. The slopes stabilize between values of $1 < d_f < 5/3$. The lower bound displays the expected dimension for strictly linear growth. The upper bound coincides with the exponent expected for a growing self-avoiding chain.²⁰ The curly appearance of the fibrils in the electron micrographs is reflected by that range of values.

The kinetic data exhibits a striking intrinsic property, as can be seen from Figure 5(a) and (b). The time t for each kinetic run is multiplied by the corresponding concentration n_1 . An approximate data collapse occurs on mastercurves. This is shown for $M_{\text{rel}}(t \cdot n_1)$ and $\theta_{\text{rel}}(t \cdot n_1)$ in Figure 5(a) and (b), respectively. This justifies the plot of θ_{rel} versus M_{rel} , which again eliminates the time-scale (Figure 5(c)). The content of β -sheet structure increases continuously with the average mass of the aggregates. Half of the secondary structure rearrangement occurs with the formation of clusters composed of ten monomers on average, correlating with the end of the first growth stage. The CD spectrum taken after 14 hours in Figure 1 corresponds to this size.

The increase in β -sheet structure levels off when an average mass of about 30 monomers per aggregate is reached. This size falls within the second growth stage, during which structures of fibrillar morphology evolve. The CD spectrum at 144 hours corresponds to this stage (Figure 1). At that time the aggregates have reached an average

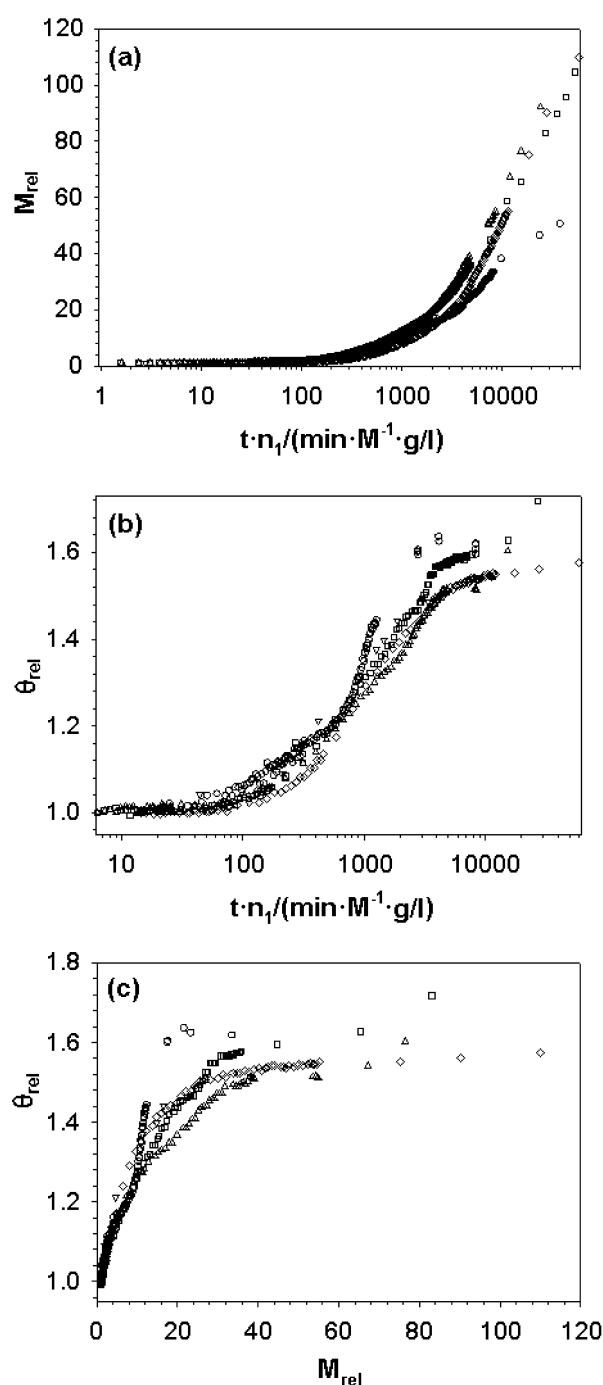


Figure 5. Dynamic scaling property of kinetic data of PGK. Concentrations were 3.3 μM (∇), 21.8 μM (\circ), 60.6 μM in $^2\text{H}_2\text{O}$ (Δ), 60.6 μM (\square) and 154.8 μM (\diamond) in each part. The SLS-data are shown in (a). M_{rel} is plotted versus the time multiplied by the corresponding concentration. The CD-data at 215 nm are shown in (b). θ_{rel} is plotted versus the time multiplied by the corresponding concentration. A good superposition of the data occurs in both cases. This justifies plotting θ_{rel} versus M_{rel} , which eliminates the time-scale, as in (c), and reveals the coupling between mass and secondary structure of protein aggregates.

mass of 33.5 monomers. These phenomenological observations demonstrate the coupling between cross β -sheet formation and amyloid growth.

So far we have identified two growth stages, two distinguished cluster sizes of ten and 30 monomers, respectively, together with a remarkable scaling property which helped to reveal the inherent coupling between internal structural changes of the protein chains and their aggregation, thus accounting for the concentration dependence. Only a closer inspection of the time-dependences and an explanation of the concentration scaling property will allow discrimination between different growth mechanisms such as sequential addition of monomers or aggregation between oligomers, and will give support for an interpretation of the marked cluster sizes. The basis for this venture is laid in the next section.

Theoretical description

A general overview of protein misassembly and aggregation phenomena is given by Jaenicke & Seckler.²¹ Smoluchowski coagulation theory, in particular, was applied only very scarcely to protein aggregation phenomena. Applications include the description of the heat aggregation of immunoglobulin (IgG),²² protein crystal growth²³ and inclusion body formation.²⁴ Until now only two studies exist which utilize Smoluchowski coagulation theory for modeling late stages of A β -amyloid growth.^{25,26} Therefore, we see the need to compile the essential framework of the theory.

Smoluchowski coagulation theory

The basic assumptions for the rate equation approach of von Smoluchowski are:^{17,18}

- The reaction rate $K_{i,j}$ for aggregation of two clusters containing i and j monomers is similar for any pair of clusters containing i and j monomers. Therefore, $K_{i,j} = K_{j,i}$, represents a configurational and orientational average for the exact reaction rate of a pair of two clusters with a specific configuration colliding under a specific orientation.
- Once two clusters have reacted with each other their bond is considered to be unbreakable. Therefore, the growth process is irreversible.
- The number concentration n_i of clusters containing i monomers can be represented by its spatial average. Thus the spatial dependence of all quantities is neglected, making this approach a mean-field type of theory.
- The solution is sufficiently diluted, so that the reaction rate $K_{i,j}$ between two clusters i and j is not affected by the presence of other clusters. Consequently reactions involving three and more clusters are omitted.

With these assumptions, Smoluchowski coagulation equation is obtained by writing the population balance equation for clusters containing k monomers, taking into account both the gains and losses due to collisions:

$$\frac{d}{dt}n_k(t) = \frac{1}{2} \sum_{i+j=k} K_{i,j}n_i(t)n_j(t) - n_k(t) \sum_{j=1}^{\infty} K_{k,j}n_j(t) \quad (1)$$

The first term on the right hand side describes the mean rate by which k -mers are formed through the reaction of i -mers with j -mers. The second term represents the loss of k -mers through the formation of larger clusters by their binding to j -mers. All physicochemical information about the aggregation mechanism is contained in the rate-constants $K_{i,j}$. The size dependence of the rate-constants can be neglected under conditions explained in Materials and Methods. Then the rate constants are given by:

$$K_{i,j} = \alpha k_s \text{ with } k_s = \frac{8k_B T}{3\eta} \quad (2)$$

The parameter α is introduced to account for regimes of slow coagulation¹⁸ where only a fraction of collisions between clusters leads to bond formation. For this reason α is named sticking probability and lies in the interval $0 < \alpha \leq 1$. Coagulation is said to take place in the diffusion-limited regime, the fastest possible regime, with the Smoluchowski rate constant k_s , if α equals one. Smoluchowski coagulation equation (1) with size-independent rate constants (2) can be solved analytically for the number concentrations n_k (see Materials and Methods). These are summed up to yield for the average cluster mass:

$$\begin{aligned} M_{\text{rel}}(t) &= \bar{n}(t)/n_1(0) = \sum_{i=1}^{\infty} i^2 n_i(t)/n_1(0) \\ &= (1 + 2t/t_c) \end{aligned} \quad (3)$$

where $t_c = 2/\alpha k_s n_1$ is the coagulation time.

We fitted equation (3) to the SLS data for the first growth stage for the different concentrations. The only free fit parameter is the coagulation time t_c . Making use of the mass scaling law for the hydrodynamic radius, yields $R_{\text{rel}}(t) = (1 + 2t/t_c)^{1/d_1}$ as the fit function, where $d_1 = 2.17$ is fixed and was derived from the first growth stage from Figure 4. This equation was fitted to DLS data for the first growth stage. The results are shown in Figure 6(a) and confirm the predicted proportionality $1/t_c \propto n_1$ of Smoluchowski's theory. Moreover, the proportionality constant is the same within the experimental scatter for the independent fits to the SLS and DLS data showing the self-consistency of the approach. The sticking probability for the first growth phase α_1 was calculated from the slope of Figure 6(a), utilizing the definition for t_c and a value of $k_s = 6.6 \times 10^9 \text{ M}^{-1} \text{ s}^{-1}$ for Smoluchowski rate constant, to be $\alpha_1 \approx 9 \times 10^{-10}$. We rescaled each kinetic run for $M_{\text{rel}}(t)$ and $R_{\text{rel}}(t)$

with the coagulation time t_c derived from the corresponding fit. The resulting mastercurves are shown in Figure 6(b) and (c). The agreement between the prediction of Smoluchowski's theory and the experimental data is, within the experimental errors, very good.

Exclusion of sequential monomer addition

The result for $M_{\text{rel}}(t)$, assuming growth by sequential addition of monomers, is shown in Figure 6(b)–(d). This mechanism is defined through the set of equations:^{22,24}

$$\begin{aligned} \frac{d}{dt}n_1(t) &= -K_{1,1}n_1^2(t) - n_1(t) \sum_{j=1}^{\infty} K_{1,j}n_j(t) \\ \frac{d}{dt}n_k(t) &= K_{1,k-1}n_1(t)n_{k-1}(t) - K_{1,k}n_1(t)n_k(t) \end{aligned} \quad (4)$$

The size-independent rate-constants given by equation (2) are chosen for the same reasons explained in Materials and Methods. The results are in direct conflict to the experimental observation. The fast depletion of monomers explains the rapid saturation of the average cluster mass $M_{\text{rel}}(t)$.^{22,24} Sequential monomer addition can thus be unambiguously ruled out as an alternative growth mechanism. This demonstrates the necessity to allow reactions between all cluster sizes which are modeled by the first term in Smoluchowski coagulation equation (1) to produce effective growth in case of irreversible reactions.

Refinement of theoretical description

The first growth phase is shown in semi-logarithmic fashion in Figure 6(d). For short times ($t/t_c < 1$) and small average masses ($M_{\text{rel}} < 3$) the solution for $M_{\text{rel}}(t)$ assuming size-independent rate-constants deviates systematically from the experimental data. The data is better fitted by an exponential time-course. Such a behavior can be explained by taking the size-dependence of the rate-constants into account. This is done in a physically reasonable way by claiming the so-called homogeneity relation:²⁷

$$K_{ai,aj} \propto a^\lambda K_{i,j} \text{ with } \lambda \leq 2 \quad (5)$$

for the rate-constants $K_{i,j}$, and a is a positive, real number. The restriction $\lambda \leq 2$ has to be applied, since otherwise the cluster reactivity would rise faster than its mass which would correspond to a non-physical situation.²⁷ The homogeneity exponent λ connects the reaction rate of two small clusters to that of two large clusters. For a positive λ the aggregation rate increases with increasing cluster sizes and decreases for negative values. Therefore, λ governs the overall time evolution of the aggregation mechanism.

Solutions of Smoluchowski coagulation equation with rate-constants $K_{i,j}$ which obey the

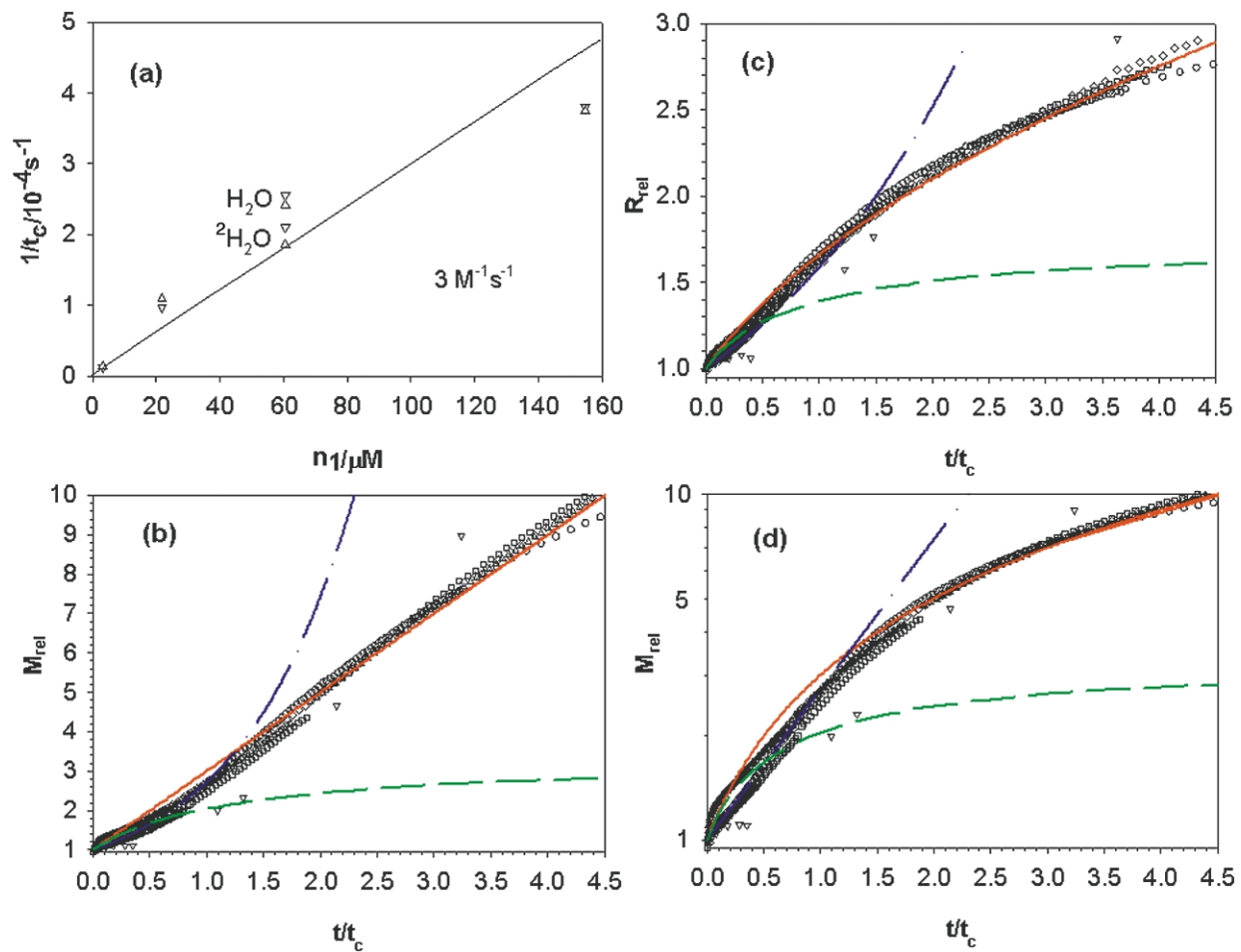


Figure 6. Application of Smoluchowski's theory to the first growth stage of PGK ($1 < M_{\text{rel}} < 10$). (a) shows the inverse coagulation time t_c^{-1} versus PGK concentration. The coagulation time was derived either by fitting equation (3) to the SLS-data (∇) or by fitting independently $R_{\text{rel}}(t) = (1 + 2t/t_c)^{1/2.17}$ to the DLS-data (Δ), shown in Figure 3(a) and (b). The slope equals $3 \text{ M}^{-1} \text{ s}^{-1}$. PGK concentrations shown in (b)–(d) were $3.3 \text{ } \mu\text{M}$ (∇), $21.8 \text{ } \mu\text{M}$ (\circ), $60.6 \text{ } \mu\text{M}$ in $^2\text{H}_2\text{O}$ (Δ), $60.6 \text{ } \mu\text{M}$ (\square) and $154.8 \text{ } \mu\text{M}$ (\diamond). M_{rel} as a function of the rescaled time t/t_c is shown in a linear (b) and semi-logarithmic (d) plots. (c) shows R_{rel} versus the rescaled time t/t_c . The red curve represents the solution of Smoluchowski's theory in (b)–(d). Sequential monomer addition is given by the green, short dashed curve in each part. The blue, dash dotted curve represents RLCA which is characterized by an exponential time-course.

homogeneity relation (5) indicate a time-dependence of the average cluster mass of the form:²⁸

$$M_{\text{rel}}(t) = (1 + 2t/t_c)^z \quad (6)$$

The exponent z is connected to the homogeneity exponent λ by $z = 1/(1 - \lambda)$.

Diffusion-limited cluster aggregation (DLCA) is given for $\lambda = 0$ and sticking probabilities, α , close to one and is the fastest possible aggregation regime. The slowest regime, called reaction-limited cluster aggregation (RLCA), is assumed to take place for $\lambda = 1$ and $\alpha \ll 1$. RLCA is characterized by an exponential time-course for the mass $M_{\text{rel}} \propto \exp[Ct]$, where C is a constant depending on the specific conditions of the system under investigation.²⁹ Intermediate values of λ belong to the so called cross-over regime (XOVER). The dynamic exponent z and thus the kernel homogeneity depend on solvent conditions such as

ionic strength and pH. Variations in these parameters can be used to tune the aggregation regime between pure DLCA and RLCA.³⁰ The physical nature and the onset of the XOVER-regime is still a matter of debate.³¹

The initial exponential time-course of M_{rel} in Figure 6(d) suggests that this very early phase falls in a RLCA-like or XOVER-regime. Latest investigations of the size-dependence of rate-constants with a homogeneity exponent $\lambda = 0$, being capable of describing a cross-over from an initial exponential to a linear time-course, point to an assignment to the XOVER regime.^{32,33}

Application of the refined description to the second growth stage

In order to analyze the second growth stage, we subtracted $4.5 \times t_c(n_1)$ from each kinetic run,

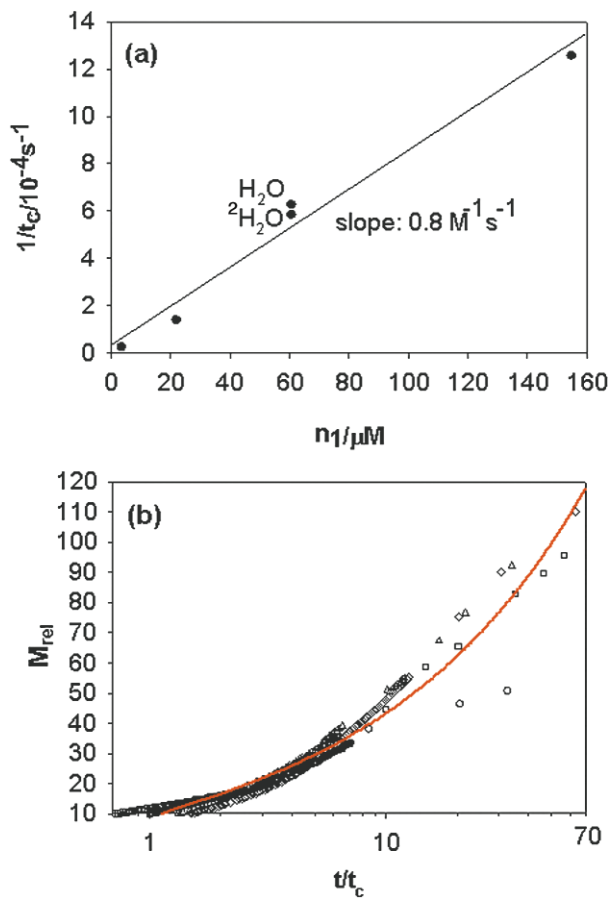


Figure 7. Application of refined Smoluchowski's theory (equation (6)) to the second growth stage of PGK ($M_{\text{rel}} > 10$). (a) shows the inverse coagulation time t_c^{-1} versus PGK concentration. M_{rel} versus t/t_c is shown in (b) for PGK concentrations of 3.3 μM (∇), 21.8 μM (\circ), 60.6 μM in $^2\text{H}_2\text{O}$ (Δ), 60.6 μM (\square) and 154.8 μM (\diamond). The curve is the fit to the rescaled data which yielded a dynamic scaling exponent $z = 0.5$. The logarithmic time axis is chosen to allow a judgement of the accuracy of the fit for short times ($t/t_c < 10$).

inserting the corresponding concentration, and rescaled the mass by the average cluster mass $M_{\text{rel}}(4.5 \times t_c) = 10$. We then fitted the data by the general form for $M_{\text{rel}}(t)$ given by equation (6). The original time for each experiment was rescaled by the coagulation time t_c derived from the fits. Again, data collapse occurs (Figure 7(b)). The theoretically predicted proportionality $t_c^{-1} \propto n_1$ is confirmed in Figure 7(a). The sticking probability for the second stage, α_2 , was calculated to be $\alpha_2 = 2.4 \times 10^{-10}$ from the corresponding slope and is thus about four times smaller than α_1 for the first growth process. The exponent z equals approximately 0.5. Therefore, the corresponding homogeneity exponent is given by $\lambda = -1$. During the second growth stage fibrils are formed. Aggregation occurs only at their tips. The encounter radius for reaction is proportional to the diameter of the fibrils and hence remains constant during reaction, whereas increasing fibril lengths result in a

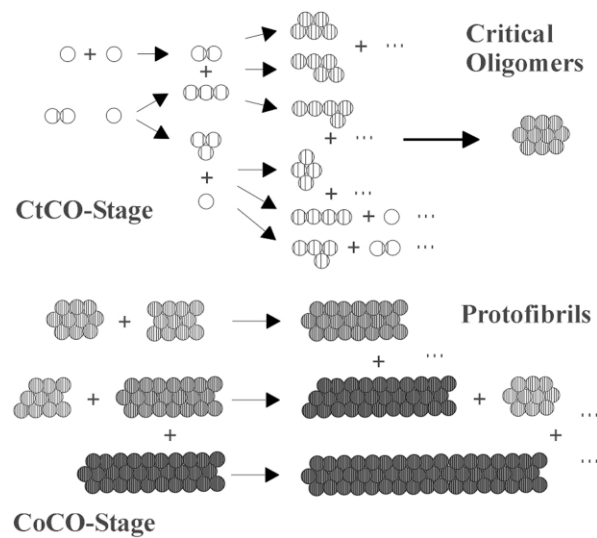


Figure 8. Model of amyloid protofibril assembly of PGK. Critical oligomers are formed during the first growth stage, called clustering, to form critical oligomers (CtCO). The circles represent monomers or monomeric subunits of the growing oligomeric protein species. The increase of β -sheet strands is symbolized by the increasing number of secants drawn within the circles during the CtCO-stage. Only some of the possible reactions according to equation (1) are shown. The actual arrangement of the circles is diagrammatic. It should be viewed as a cartoon of the oligomer configurations appearing in solution throughout the aggregation process. The critical oligomers then assemble to protofibrils. This second growth stage is termed CoCO. Further increase in cross β -sheet structure is indicated by the increasing gray-shadings. Protofibrils are drawn straight due to space limitations. Their virtually curly appearance can be seen in Figure 2.

decrease of the diffusion coefficient. Both effects taken together lead to a decrease in the rate-constants with growing length of the fibrils. This can be understood formally through the equation for rate-constants of Brownian particles given in Materials and Methods. The negative value of the rate-constants homogeneity exponent λ corroborates this.

Discussion

Considering the findings concerning the assembly states, we derive the model shown in Figure 8 for the amyloid formation of PGK. The first growth stage takes place *via* clustering in a XOVER regime. It is characterized by a low sticking probability $\alpha_1 = 9 \times 10^{-10}$ and a growth exponent $d_1 = 2.17 \pm 0.09$. The process lasts ~ 4.5 times the coagulation time t_c . The oligomers have an average mass of ten monomeric units.

During the second growth stage structures of fibrillar morphology arise. The aggregated species are short curved fibrils. They are formed by coalescing of the oligomers supplied by the first growth

stage. They are between 50 nm and 150 nm long. These values are estimates from the electron micrographs and the hydrodynamic radii which were converted to lengths by assuming rigid rods of 8 nm.³⁴ The kinetics are characterized by a continuously decreasing reaction rate between the growing species and a sticking probability $\alpha_2 = 2.4 \times 10^{-10}$.

Magnitude of sticking probability

The bimolecular rate-constants for both growth stages are about ten orders of magnitude smaller than the diffusion-limited Smoluchowski rate, translating to sticking probabilities of the order of $\alpha \approx 10^{-10}$. The sticking probability for the heat aggregation of IgG was found to lie in the same range.²²

In comparison hitherto, protein–protein bond formations, such as antibody–antigen complexation, occur usually with sticking probabilities in the order of $\alpha \approx 10^{-3}$.³⁵ In these cases the reaction partners possess a rather defined tertiary structure and the reactive patches at their surfaces are largely preformed, whereas the initial state of PGK represents a large ensemble of conformations without defined tertiary contacts. One plausible interpretation for the six to seven orders of magnitude smaller sticking probability is that only a small fraction of the members of the initial ensemble is aggregation-competent.

A supplemental view is given by the notion of fluctuating secondary structure elements, so-called microdomains, known from the diffusion–collision model of protein folding.³⁶ The small sticking probability is then interpreted as a sign of the low probability of coalescence of two microdomains which are contained in different protein molecules. In this context the microdomains are non-native structures, short β -sheet strands, which are stabilized by intermolecular coalescence. This interpretation represents an extension of the diffusion–collision model³⁶ to misfolding of proteins, whereby the crucial point is the stabilization of misfolded secondary structure elements (microdomains) through quaternary contact formation.

Coupling of growth and conformational conversion

As shown in Figure 5(c) the conversion to β -sheet structure monitored by θ_{rel} is strictly monoton increasing with the mass M_{rel} and *vice versa*, including the very beginning with small values of M_{rel} . This is shown schematically in Figure 8, where the β -sheet content within a monomeric subunit increases with the number of subunits per oligomer, supporting the dynamic picture of stabilization of misfolded microdomains by intermolecular coalescence.

As more and more protein chains accumulate in a predominant β -sheet structure within the oligomers an extended cross β -sheet structure is

formed. This results in a structural polarity of the aggregates exceeding a certain size. Consequently further growth takes place in a linear fashion. Therefore, we term the aggregates critical oligomers and the first growth stage clustering towards critical oligomers (CtCO). At this point half of the overall change in ellipticity has occurred.

The ellipticity signal saturates within the second growth stage when the critical oligomer coalesces to form short fibrils. Similar intermediate fibrillar aggregates have been found in the case of other proteins, including A β ,^{37,38} transthyretin (TTR) and variants,^{39,40} α -synuclein,⁴¹ NM¹² and β_2 -microglobulin.⁴² As tribute to the discoverers we name this species according to their proposal protofibrils.^{37,38} In principle, growth occurs by the clustering of all available critical oligomers and protofibrils. We term this whole stage clustering of critical oligomers (CoCO).

The found coupling of growth and conformational conversion demonstrates the fundamental differences between protein and colloid aggregation phenomena, where in the latter case the primary particles possess no internal structure and degrees of freedom.

In general terms, the amyloid formation of PGK has been found to be an irreversible, two step process with an on-pathway intermediate. The critical oligomers represent the pivotal point from which protofibrils arise.

Relation to other *in vitro* studies

A ladder of quaternary structural intermediates prior to protofibril assembly was observed in case of TTR and its variants,³⁹ reminiscent of the CtCO-stage of PGK. The oligomeric intermediates fall in the molecular mass range of 14,000, the size of the monomer, to 260,000.

Studies of the aggregation behavior of hamster PrP(27–30), recombinant hamster PrP(90–231), and recombinant huPrP(90–231) yield a picture which broadly matches the CtCO-stage on a qualitative basis.^{43,44} Acquisition of β -sheet structure occurs concomitantly with oligomerization.

The formation of protofibrils through fusion and further addition of oligomeric protein species was observed directly for amyloid fibrils of A β ⁴⁵ and the NM-construct of Sup35^{11,12} by atomic force measurements. Xu *et al.*¹² hypothesized that the observed aggregation behavior may be analogous to linear colloidal aggregation. The quantitative description of the CoCO-stage of PGK protofibril formation can be seen to corroborate this speculation. The elongation rate of protofibrils depends linearly on the protein concentration in case of A β protofibrils.⁴⁶ This is confirmed by the present study. On the basis of light-scattering data, A β -amyloid fibril elongation was modeled as a DLCA-process.²⁵ But A β -amyloid fibril growth was also observed in a RLCA-regime.²⁶ This reflects the dependence of the aggregation kinetics on solvent conditions. This is in accordance with

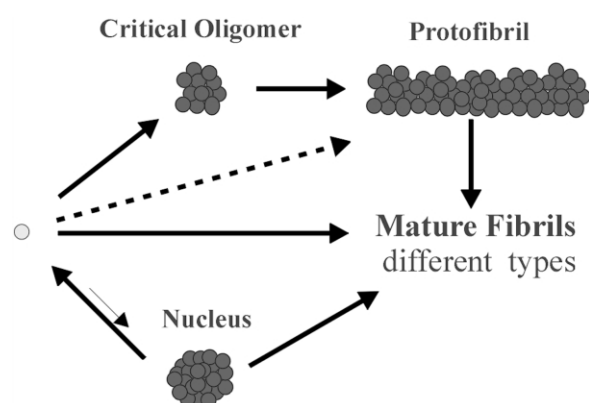


Figure 9. Overview of amyloid fibril formation. The findings of this study together with the quoted literature can only be explained consistently by assuming parallel pathways of amyloid formation. The upper pathway is given through the formation of critical oligomers. These possess a conformation which gives rise to a structural polarity. Thus further growth occurs through fusion of critical oligomers to protofibrils in a linear fashion. Protofibrils can transform to mature fibrils. The lower pathway is characterized by a nucleation event which is the rate-limiting step. The nuclei grow by addition of monomers to mature fibrils. Mature fibrils and perhaps protofibrils serve as templates for the partially folded monomers symbolized by the bright shaded circle. Growth occurs then by adding directly monomers to these structures analogous to heterogeneous nucleation. It has to be stressed that the ensemble of partially folded monomers at the start of each reaction pathway does not have to be identically. Conformational preferences for a certain pathway to become active might exist. In this respect influence of environmental conditions such as pH, temperature and salt has to be considered. Changes of them might allow switching between pathways.

Smoluchowski's theory, in which these dependencies enter through the homogeneity exponent λ of the rate constants.

Therefore, we evaluate our experimental findings and those from the studies cited above as a strong evidence that protofibril formation in general is a two stage process where oligomeric species are formed in a first stage which coalesce to protofibrils in a second growth stage. This pathway is shown in Figure 9.

Further on we propose that our specific description according to the CtCO- and CoCO-stage (Figure 8) might represent one mode of this general pathway applicable to a broader class of amyloidogenic proteins.

Discussion of pathways

Serio *et al.* describe the reaction from the initial monomeric state to the oligomeric species shown in Figure 9 for the NM construct of the yeast prion protein-determinant Sup35 as a reversible reaction. First, the NM oligomers formed are unstructured and in a somewhat fluid-like state. Afterwards the conformational transition to a β -sheet rich oligomer occurs in a cooperative manner; there-

fore, the term NCC.¹¹ The NCC model is in marked contrast to the CtCO-stage for PGK, where growth and conformational conversion are diffusion-collisional coupled events. Both models might represent limiting cases for the initial oligomerization reaction shown in Figure 9 and intermediate behavior might exist. The reversibility of the reaction, assumed in the NCC-model, reflects the special molecular biology of yeast prions, which allows yeast cells to switch between the $[\text{PSI}^+]$ and the $[\text{psi}^-]$ -state.¹¹

Protofibrils can transform further to mature fibrils as indicated in Figure 9. Mature fibrils are more straight than protofibrils and show different morphologies.⁴⁷ Two main morphologies are reported, multistranded ribbons and coiled fibrils, consisting of intertwined protofibrils.⁴⁸ Kad *et al.* found no mature fibrils under the conditions where protofibrils are formed for β_2 -microglobulin.⁴² But they could produce mature fibrils without detectable protofibrils under different solution conditions. So far we have found no indication for a transition of protofibrils to mature fibrils in the case of PGK. The transition itself and the environmental influences are characterized very poorly in the existing model systems.

Generally, nucleated polymerization⁷ is used as mechanism to explain fibrillogenesis which is shown in Figure 9 as the lower branch leading to mature fibrils. This assumption is mainly on the basis of three criterions, a critical concentration for start of polymerization reaction, the observation of a lag phase, and that seeding with fibrils abolishes the lag phase.⁸ Seeding is a pathway of its own for elongation of mature fibrils equivalent to heterogeneous nucleation (see Figure 9) but it cannot explain fibril formation.

Other mechanisms might meet these phenomenological criterions, too. The most outstanding feature of an NP mechanism is the concentration dependence of the nucleation rate k_{nuc} . It is given through $k_{\text{nuc}} \sim c^{n/2} \sim 1/t_{\text{lag}}$ with n strictly being larger than two.⁴⁹ The exponent n denotes the number of monomers building up the nucleus and t_{lag} is a measure for the duration of the lag phase. This feature unambiguously distinguishes an NP-mechanism from other aggregation phenomena like the CtCO-stage of PGK where n equals two. Unfortunately, this criterion is used in the fewest studies.⁴⁷

We want to stress the fundamental difference in the physical nature of the nucleus on the NP pathway and the critical oligomers and protofibrils shown in Figure 9. The nucleus is the least stable species on an NP-pathway, forming the rate-limiting bottleneck which is stabilized through addition of further monomers.⁴⁹

Serio *et al.* raised the possibility that protofibrils can grow additionally through monomer addition like mature fibrils.¹¹ This proposal is on the basis of seeding experiments but without closer characterization of the used seeds. Xu *et al.* found protofibrils and mature fibrils under the same

conditions¹² as those used by Serio *et al.* to prepare their seeds.¹¹ In the case of A β , e.g. protofibrils show no acceleration of the kinetics in seeding experiments,⁵⁰ disproving the assumption of monomer addition to protofibrils. Therefore, the assumption of heterogeneous nucleation of protofibrils is rather speculative and the arrow is drawn dashed in Figure 9.

The exact relation of the pathways *via* an NP-mechanism or *via* oligomers and protofibrils to mature fibrils has to be worked out in the future. So far it is unclear if these pathways are parallel or if only one of them exists for any given protein. Switching between these pathways might be possible through environmental influences like suitable solution conditions.

Conclusion

The proposed model of protofibril formation is a two step process. During the first step, clustering towards critical oligomers occurs (CtCO-stage). Protofibrils are formed throughout the second step by clustering of critical oligomers (CoCO-stage) provided by the first step. Acquisition of β -sheet structure and growth are coupled events. The coupling might be mediated through collisions between flickering microdomains, which are stabilized in a β -sheet conformation through intermolecular coalescence. The kinetics of both steps are found to be irreversible. Both growth stages can be very well described within the framework of Smoluchowski's coagulation theory. This suggests that amyloid protofibril formation of PGK can be viewed as a process under kinetic control far away from thermodynamic equilibrium.

The proposed model can serve as a tool to make oligomeric intermediates accessible for closer biochemical and biophysical characterization. This could be achieved by manipulating the sticking probabilities of the two growth stages. Use of appropriate solution conditions may substantially lower the sticking probability of the CoCO-stage. Thus aggregation of critical oligomers is essentially prevented, so that the population of critical oligomers formed by the CtCO-stage is enriched and kinetically stabilized without noticeable interference on a long time-scale. This is of tremendous importance, because on-pathway intermediates of fibrillogenesis are supposed to be neurotoxic, causing cell death and disease. A recent study showed that such protein species are able to destroy the membrane of synthetic vesicles,⁵¹ stressing the last point.

Materials and Methods

Yeast 3-phosphoglycerate kinase (EC 2.7.2.3) was purchased from Boehringer Mannheim GmbH (Germany). All other chemicals were of analytical grade.

Preparation of native PGK

The ammonium sulphate precipitated protein was pelleted and then dissolved in 20 mM sodium phosphate buffer (pH 6.5), 1 mM EDTA, 1 mM DTT. Insoluble material was removed by centrifugation. Subsequently the supernatant was exhaustively dialyzed against the same buffer. Homogeneity of the preparation was checked by applying an aliquot to an FPLC-Superose 12 column (Pharmacia LKB Biotechnology, Sweden). Only one symmetric peak was detected without any indication of aggregated protein.

Preparation of start conformation of PGK

PGK in 20 mM sodium phosphate buffer (pH 6.5), 1 mM EDTA was exhaustively dialyzed against 10 mM HCl (pH 2). This solution was mixed with appropriate volumes of concentrated solutions of NaCl in 10 mM HCl (pH 2) prior to initiation of the kinetic runs.

Protein concentrations

PGK concentrations were determined spectro-photometrically using $A_{1\text{ cm}}^{1\%} = 4.95$ at 280 nm.⁵²

Circular dichroism

CD measurements were performed at 20 °C on a Jasco J-720 spectrometer (Japan) in 0.1 mm or 1 mm cells. The spectrometer was calibrated with (+)-10 camphorsulfonic acid at 290.5 nm and 192.5 nm.⁵³ Mean residue ellipticities were calculated using a value of 107.4 for the mean residue weight of PGK.

Light-scattering

The laboratory-built LS spectrometer has been described.⁵⁴ It consists mainly of an argon laser LEXEL 3500 (Lexel Laser Inc., USA) operating at $\lambda = 514.5$ nm, a thermostated cell holder, a detection system and a 90-channel multibit multiple- τ correlator which calculates the homodyne autocorrelation function $G^2(\tau)$. All experiments were done at 20 °C and a scattering of 90° using flow-through microcells with a sample volume of 100 μ l (Hellma, Germany). Solvents and protein solutions were filtered through 100 nm pore size Anotop 10 filters (Whatman, UK) directly into the scattering cells. The laser power was 0.2–1 W. The translational diffusion coefficients, D ; were calculated from the autocorrelation functions using the program CONTIN^{55,56} or by the method of cumulants.⁵⁷ The latter was especially applied when the aggregation process was monitored using the technique of kinetic DLS. The principle and details of this technique have been described.^{54,58} Solvent viscosities were determined using an Ubbelohde type viscometer Viscoboy 2 (Lauda, Germany) and densities using a digital density meter DMA 58 (Anton Paar, Austria).

The scattered intensity, I_s , was monitored continuously at an angle of 90°. The molar masses of the protein species were calculated from their scattering intensity over that of the solvent using toluene as a scattering standard.

Electron microscopy

PGK samples were diluted in 10 mM HCl (pH 2), 190 mM NaCl to about 0.3 μ M and prepared for electron microscopy using a double carbon film technique and 1% uranyl formate as negative stain. Copper grids of 400 mesh covered with a carbon-coated holey plastic film were used as support. Micrographs were taken with an EM 910 (LEO, Germany) operating at 80 kV acceleration voltage and a nominal magnification of 63,000 \times .

Numerical calculations and simulations

The rate-constants $K_{i,j}$ for particles undergoing Brownian diffusion are given by:

$$K_{i,j} = 4\pi(R_i + R_j)(D_i + D_j)$$

where R_i stands for the geometrical radius and D_i for the diffusion coefficient of a particle containing i primary particles.¹⁸

It is a convenient approach to incorporate the size-dependence i of the rate-constants $K_{i,j}$ by assuming scaling laws for the geometrical radius $R_i = R_1 i^{1/d_t}$ and the diffusion coefficient $D_i = k_B T / 6\pi\eta R_i = k_B T i^{-1/d_h} / 6\pi\eta R_1$. The exponents d_t and d_h characterize the geometrical and hydrodynamic properties of the particles. Smoluchowski coagulation equation was solved numerically using the software package Mathematica 4.0 (Wolfram Research). The derived solutions for $n_i(t)$ and $\bar{n}(t)$ did not deviate more than 5% during the needed time-interval from the solutions assuming size-independent rate-constants (equation (2)) using appropriate exponents d_t and d_h . This justifies the use of size-independent rate-constants as approximation. These solutions are given by¹⁸ $n_i(t) = n_1(0)(t/t_c)^{i-1} / (1 + t/t_c)^{i+1}$.

Simple fits were done by the aid of the software SigmaPlot (Jandel Scientific).

Acknowledgements

The authors thank D. Zirwer for his support and CD measurements. The authors are grateful to H. Damaschun and H. Fabian for critical reading of the manuscript. We thank R. H. Pain for his thorough comments and corrections. This work was supported by the Deutsche Forschungsgemeinschaft (Da 292/6-2, He 1318/18-2, GK 268) and by a grant from the Fonds der Chemischen Industrie to G.D.

References

1. Fink, A. L. (1998). Protein aggregation: folding aggregates, inclusion bodies and amyloid. *Fold. Des.* **3**, R9–R23.
2. Pepys, M. B. (2001). Pathogenesis, diagnosis and treatment of systemic amyloidosis. *Philos. Trans. R. Soc. ser. B*, **356**, 203–210.
3. Prusiner, S. B. (2001). Shattuck lecture—neurodegenerative diseases and prions. *N. Engl. J. Med.* **344**, 1516–1526.
4. Gerlai, R. (2001). Alzheimer's disease: beta-amyloid hypothesis strengthened! *Trends Neurosci.* **24**, 199.
5. Goldberg, M. S. & Lansbury, P. T., Jr (2000). Is there a cause-and-effect relationship between alpha-synuclein fibrillization and Parkinson's disease? *Nature Cell Biol.* **2**, E115–E119.
6. Soto, C. (2001). Protein misfolding and disease; protein refolding and therapy. *FEBS Letters*, **498**, 204–207.
7. Oosawa, F. & Asakura, S. (1975). *Thermodynamics of the Polymerization of Protein*, Academic Press, London.
8. Jarrett, J. T. & Lansbury, P. T., Jr (1993). Seeding one-dimensional crystallization of amyloid: a pathogenic mechanism in Alzheimer's disease and scrapie? *Cell*, **73**, 1055–1058.
9. Prusiner, S. B. (1991). Molecular biology of prion diseases. *Science*, **252**, 1515–1522.
10. Eigen, M. (1996). Prionics or the kinetic basis of prion diseases. *Biophys. Chem.* **63**, A1–A18.
11. Serio, T. R., Cashikar, A. G., Kowal, A. S., Sawicki, G. J., Moslehi, J. J., Serpell, L. *et al.* (2000). Nucleated conformational conversion and the replication of conformational information by a prion determinant. *Science*, **289**, 1317–1321.
12. Xu, S., Bevis, B. & Arnsdorf, M. F. (2001). The assembly of amyloidogenic yeast sup35 as assessed by scanning (atomic) force microscopy: an analogy to linear colloidal aggregation? *Biophys. J.* **81**, 446–454.
13. Klein, W. L., Krafft, G. A. & Finch, C. E. (2001). Targeting small Abeta oligomers: the solution to an Alzheimer's disease conundrum? *Trends Neurosci.* **24**, 219–224.
14. Chiti, F., Webster, P., Taddei, N., Clark, A., Stefani, M., Ramponi, G. & Dobson, C. M. (1999). Designing conditions for *in vitro* formation of amyloid protofibrils and fibrils. *Proc. Natl Acad. Sci. USA*, **96**, 3590–3594.
15. Damaschun, G., Damaschun, H., Gast, K. & Zirwer, D. (1999). Proteins can adopt totally different folded conformations. *J. Mol. Biol.* **291**, 715–725.
16. Damaschun, G., Damaschun, H., Fabian, H., Gast, K., Krober, R., Wiese, M. & Zirwer, D. (2000). Conversion of yeast phosphoglycerate kinase into amyloid-like structure. *Proteins: Struct. Funct. Genet.* **39**, 204–211.
17. Smoluchowski, M. V. (1916). Drei Vorträge über Diffusion, Brownsche Molekularbewegung und Koagulation von Kolloidteilchen. *Phys. Z.* **17**, 557–599.
18. Smoluchowski, M. V. (1917). Versuch einer mathematischen Theorie der Koagulationskinetik kolloider Lösungen. *Z. Phys. Chem.* **92**, 129–168.
19. Vicsek, T. (1992). *Fractal Growth Phenomena*, World Scientific, Singapore.
20. de Gennes, P. G. (1979). *Scaling Concepts in Polymer Physics*, Cornell University Press, Ithaca, New York.
21. Jaenicke, R. & Seckler, R. (1997). Protein misassembly *in vitro*. *Advan. Protein Chem.* **50**, 1–59.
22. Jossang, T., Feder, J. & Rosenqvist, E. (1985). Heat aggregation kinetics of human IgG. *J. Chem. Phys.* **82**, 574–589.
23. Umbach, P., Georgalis, Y. & Saenger, W. (1998). Time-resolved small-angle static light scattering on lysozyme during nucleation and growth. *J. Am. Chem. Soc.* **120**, 2382–2390.
24. Speed, M. A., King, J. & Wang, D. I. C. (1997). Polymerization mechanism of polypeptide chain aggregation. *Biotechnol. Bioeng.* **54**, 333–343.

25. Tanski, S. J. & Murphy, R. M. (1992). Kinetics of aggregation of synthetic beta-amyloid peptide. *Arch. Biochem. Biophys.* **294**, 630–638.
26. Thunecke, M., Lobbia, A., Kosciessa, U., Dyrks, T., Oakley, A. E., Turner, J. *et al.* (1998). Aggregation of A beta Alzheimer's disease-related peptide studied by dynamic light scattering. *J. Pept. Res.* **52**, 509–517.
27. Ernst, M. H. (1986). Kinetics of clustering in irreversible aggregation. In *Fractals in Physics* (Pietronero, L. & Tosatti, E., eds), pp. 289–302, Elsevier, Amsterdam.
28. Olivier, B. J. & Sorensen, C. M. (1990). Variable aggregation rates in colloidal gold—kernel homogeneity dependence on aggregant concentration. *Phys. Rev. sect. A*, **41**, 2093–2100.
29. Lin, M. Y., Lindsay, H. M., Weitz, D. A., Ball, R. C., Klein, R. & Meakin, P. (1989). Universality in colloid aggregation. *Nature*, **339**, 360–362.
30. Asnaghi, D., Carpineti, M., Giglio, M. & Sozzi, M. (1992). Coagulation kinetics and aggregate morphology in the intermediate regimes between diffusion-limited and reaction-limited cluster aggregation. *Phys. Rev. sect. A*, **45**, 1018–1023.
31. Odriozola, G., Tirado-Miranda, M., Schmitt, A., Lopez, F. M., Callejas-Fernandez, J., Martinez-Garcia, R. & Hidalgo-Alvarez, R. (2001). A light scattering study of the transition region between diffusion- and reaction-limited cluster aggregation. *J. Colloid Interface Sci.* **240**, 90–96.
32. Schmitt, A., Odriozola, G., Moncho-Jorda, A., Callejas-Fernandez, J., Martinez-Garcia, R. & Hidalgo-Alvarez, R. (2000). Multiple contact kernel for diffusionlike aggregation. *Phys. Rev. sect. E*, **62**, 8335–8343.
33. Odriozola, G., Moncho-Jorda, A., Schmitt, A., Callejas-Fernandez, J., Martinez-Garcia, R. & Hidalgo-Alvarez, R. (2001). A probabilistic aggregation kernel for the computer-simulated transition from DLCA to RLCA. *Europhys. Letters*, **53**, 797–803.
34. Garcia de la Torre, J. G. & Bloomfield, V. A. (1981). Hydrodynamic properties of complex, rigid, biological macromolecules: theory and applications. *Q. Rev. Biophys.* **14**, 81–139.
35. Northrup, S. H. & Erickson, H. P. (1992). Kinetics of protein–protein association explained by Brownian dynamics computer simulation. *Proc. Natl Acad. Sci. USA*, **89**, 3338–3342.
36. Karplus, M. & Weaver, D. L. (1994). Protein folding dynamics: the diffusion–collision model and experimental data. *Protein Sci.* **3**, 650–668.
37. Harper, J. D., Wong, S. S., Lieber, C. M. & Lansbury, P. T. (1997). Observation of metastable A beta amyloid protofibrils by atomic force microscopy. *Chem. Biol.* **4**, 119–125.
38. Walsh, D. M., Lomakin, A., Benedek, G. B., Condron, M. M. & Teplow, D. B. (1997). Amyloid beta-protein fibrillogenesis. Detection of a protofibrillar intermediate. *J. Biol. Chem.* **272**, 22364–22372.
39. Lashuel, H. A., Lai, Z. H. & Kelly, J. W. (1998). Characterization of the transthyretin acid denaturation pathways by analytical ultracentrifugation: implications for wild-type, V30M, and L55P amyloid fibril formation. *Biochemistry*, **37**, 17851–17864.
40. Lashuel, H. A., Wurth, C., Woo, L. & Kelly, J. W. (1999). The most pathogenic transthyretin variant, L55P, forms amyloid fibrils under acidic conditions and protofilaments under physiological conditions. *Biochemistry*, **38**, 13560–13573.
41. Conway, K. A., Harper, J. D. & Lansbury, P. T. (2000). Fibrils formed *in vitro* from alpha-synuclein and two mutant forms linked to Parkinson's disease are typical amyloid. *Biochemistry*, **39**, 2552–2563.
42. Kad, N. M., Thomson, N. H., Smith, D. P., Smith, D. A. & Radford, S. E. (2001). Beta(2)-microglobulin and its deamidated variant, N17D form amyloid fibrils with a range of morphologies *in vitro*. *J. Mol. Biol.* **313**, 559–571.
43. Post, K., Pitschke, M., Schafer, O., Wille, H., Appel, T. R., Kirsch, D. *et al.* (1998). Rapid acquisition of beta-sheet structure in the prion protein prior to multimer formation. *Biol. Chem.* **379**, 1307–1317.
44. Jansen, K., Schafer, O., Birkmann, E., Post, K., Serban, H., Prusiner, S. B. & Riesner, D. (2001). Structural intermediates in the putative pathway from the cellular prion protein to the pathogenic form. *Biol. Chem.* **382**, 683–691.
45. Blackley, H. K. L., Sanders, G. H. W., Davies, M. C., Roberts, C. J., Tendler, S. J. B. & Wilkinson, M. J. (2000). *In situ* atomic force microscopy study of beta-amyloid fibrillization. *J. Mol. Biol.* **298**, 833–840.
46. Harper, J. D., Wong, S. S., Lieber, C. M. & Lansbury, P. T. (1999). Assembly of A beta amyloid protofibrils: an *in vitro* model for a possible early event in Alzheimer's disease. *Biochemistry*, **38**, 8972–8980.
47. Rochet, J. C. & Lansbury, P. T. (2000). Amyloid fibrillogenesis: themes and variations. *Curr. Opin. Struct. Biol.* **10**, 60–68.
48. Goldsberry, C. S., Wirtz, S., Muller, S. A., Sunderji, S., Wicki, P., Aeby, U. & Frey, P. (2000). Studies on the *in vitro* assembly of a beta 1–40: implications for the search for a beta fibril formation inhibitors. *J. Struct. Biol.* **130**, 217–231.
49. Ferrone, F. A. (1999). Analysis of protein aggregation kinetics. *Methods Enzymol.* **309**, 256–274.
50. Harper, J. D., Lieber, C. M. & Lansbury, P. T., Jr (1997). Atomic force microscopic imaging of seeded fibril formation and fibril branching by the Alzheimer's disease amyloid-beta protein. *Chem. Biol.* **4**, 951–959.
51. Volles, M. J., Lee, S. J., Rochet, J. C., Shtilerman, M. D., Ding, T. T., Kessler, J. C. & Lansbury, P. T., Jr (2001). Vesicle permeabilization by protofibrillar alpha-synuclein: implications for the pathogenesis and treatment of Parkinson's disease. *Biochemistry*, **40**, 7812–7819.
52. Adams, B., Burgess, R. J. & Pain, R. H. (1985). The folding and mutual interaction of the domains of yeast 3-phosphoglycerate kinase. *Eur. J. Biochem.* **152**, 715–720.
53. Johnson, W. C., Jr (1990). Protein secondary structure and circular dichroism: a practical guide. *Proteins: Struct. Funct. Genet.* **7**, 205–214.
54. Gast, K., Damaschun, G., Misselwitz, R. & Zirwer, D. (1992). Application of dynamic light scattering to studies of protein folding kinetics. *Eur. Biophys. J.* **21**, 357–362.
55. Provencher, S. W. (1982). Contin—a general-purpose constrained regularization program for inverting noisy linear algebraic and integral-equations. *Comp. Phys. Commun.* **27**, 229–242.
56. Provencher, S. W. (1982). A constrained regularization method for inverting data represented by linear algebraic or integral equations. *Comp. Phys. Commun.* **27**, 213–227.
57. Koppel, D. E. (1972). Analysis of macromolecular polydispersity in intensity correlation spectroscopy:

- the method of cumulants. *J. Chem. Phys.* **57**, 4814–4820.
58. Gast, K., Nöppert, A., Müller-Frohne, M., Zirwer, D. & Damaschun, G. (1997). Stopped-flow dynamic light scattering as a method to monitor compaction during protein folding. *Eur. Biophys. J.* **25**, 211–219.

Edited by R. Huber

(Received 21 May 2002; received in revised form 7 October 2002; accepted 10 October 2002)